DE GRUYTER Green Processing and Synthesis 2023; 12: 20230065

Research Article

Ting Wang, Junpeng Tan, Shenghui Xu, Yong Li, and Hongxia Hao*

Studies on the extraction performance of phorate by aptamer-functionalized magnetic nanoparticles in plasma samples

https://doi.org/10.1515/gps-2023-0065
received April 12, 2023; accepted October 9, 2023

Abstract: Phorate, a highly toxic organophosphorus pesticide, poses significant risks due to its efficiency, versatility, and affordability. Therefore, studying pretreatment and detection methods for phorate in complex samples is crucial. In this study, we synthesized core-shell phorate aptamer-functionalized magnetic nanoparticles using solvothermal and self-assembly techniques. Subsequently, we developed a magnetic dispersive solid-phase extraction and detection method to identifying phorate in plasma samples. Under optimal conditions, we achieved quantitation of phorate within a range of 2–700 ng·mL^{-1} using gas chromatography-mass spectrometry. The detection limit ($S/N = 3$) was 0.46 ng·mL^{-1}, and the intraday and interday relative standard deviation were 3.4% and 4.1%, respectively. In addition, the material exhibited excellent specificity, an enrichment capacity (EF = 416), and reusability (≥15). During phorate extraction from real plasma samples, spiked recoveries ranged from 86.1% to 101.7%. These results demonstrate that our method offers superior extraction efficiency and detection capability for phorate in plasma samples.

Keywords: phorate, magnetic nanoparticle, aptamer, magnetic solid phase extraction

1 Introduction

Phorate, scientifically known as *O*,*O*-diethyl-*S*-(ethylthiomethyl) dithiophosphate, possesses the ability to inhibit acetylcholinesterase activity in organisms, leading to neurological dysfunction [1]. This highly toxic organophosphorus pesticide (OPP) is unfortunately often misused in crop cultivation due to its efficiency, versatility, long-lasting effects, and cost-effectiveness. Consequently, it has resulted in numerous cases of poisoning among humans and animals [2]. Furthermore, incidents of suicide and homicide involving phorate have become significant societal concerns [3–5]. Thus, it is imperative to qualitatively and quantitatively determine the presence of phorate in biological samples to study and assess poisoning cases and provide appropriate follow-up treatment to affected individuals.

In recent years, researchers have placed significant focus on investigating extraction and determination methods for phorate in complex biological samples, with particular emphasis on the extraction methodology [6–9]. Magnetic solid-phase extraction (MSPE) represents a promising approach in dispersive solid-phase extraction that utilizes magnetic nanoparticles (MNPs) as adsorbent substrates [10]. This method facilitates rapid analyte separation between the sorbent and substrate via an external magnetic field, effectively eliminating the shortcomings associated with traditional sample pretreatment techniques, such as the extensive use of organic solvents, specialized equipment, and labor-intensive, time-consuming processing [11–13]. Moreover, it streamlines the process by eliminating the need for additional centrifugation or filtration. MSPE adsorbents are environmentally friendly, offer a substantial specific surface area, exhibit excellent compatibility, and are reusable. Owing to their outstanding adsorption and extraction performance, as well as their ease of surface modification to

---

*** Corresponding author: Hongxia Hao,** Key Laboratory of Evidence Science (China University of Political Science and Law), Ministry of Education, Collaborative Innovation Center of Judicial Civilization, Beijing, 100088, China, e-mail: tiejp_hhx@163.com

Ting Wang: Key Laboratory of Evidence Science (China University of Political Science and Law), Ministry of Education, Collaborative Innovation Center of Judicial Civilization, Beijing, 100088, China; Chemistry Department, College of Science, Hebei North University, Zhangjiakou, 075000, Hebei, China

Junpeng Tan: Key Laboratory of Evidence Science (China University of Political Science and Law), Ministry of Education, Collaborative Innovation Center of Judicial Civilization, Beijing, 100088, China; Physical and Chemical Laboratory, Institute of Forensic Science, Zhangjiakou Municipal Public Security Bureau, Zhangjiakou, 075000, Hebei, China

Shenghui Xu, Yong Li: Physical and Chemical Laboratory, Institute of Forensic Science, Zhangjiakou Municipal Public Security Bureau, Zhangjiakou, 075000, Hebei, China

enhance versatility and selectivity, MSPE has emerged as a popular approach for investigating phorate and other OPPs [14–17].

MSPE adsorbents can modify their chemical properties through surface enhancements using functional materials, thereby increasing stability and introducing new functional groups to enhance target adsorption capacity [18–22]. Researchers have employed functionalized MNPs as adsorbents for phorate extraction from samples. For example, Tang et al. [23] synthesized γ-Fe_2O_3/chitosan magnetic microspheres for extracting 10 OPP residues, including phorate, from fruits. Mahpishanian and Sereshti [24] utilized graphene (G) to craft 3D nanoporous 3D-G-Fe_3O_4 aerogels to extract phorate from fruit juice. Li et al. [25] used metal-organic framework materials to prepare magnetic nanoporous carbon materials, enabling the extraction of OPPs through π–π and hydrophobic interactions. These methodologies showed commendable extraction performance and yielded acceptable recoveries. Nevertheless, they exhibited limited specificity, compromised enrichment factors (EFs), and primarily underwent testing with uncomplicated sample matrices. Consequently, the exploration of new functionalized magnetic adsorbents is warranted to address these shortcomings.

Aptamers (Apt), comprising single-stranded oligonucleotide chains with specific sequences selected through the systematic evolution of ligands via exponential enrichment [26], present a distinctive opportunity. They can specifically bind to target substances [27], offering attributes such as high affinity, robust specificity, minimal molecular weight, *in vitro* selectivity, nonimmunogenicity, ease of modification, and excellent biocompatibility [28–30]. Apt, in comparison to antibodies, possesses a wider range of applications in biology [31], medicine [32], safety [33], environment [34], and other domains. Recent advances in aptamer technology have led to the selection or design of aptamer nucleic acid sequences with increased affinity and specificity for phorate. This has expanded the realm of possibilities for phorate extraction and detection methods. Wang et al. [35], for instance, employed ssDNA Apt for four OPPs, including phorate, and developed a method based on molecular beacon probes with a dissociation constant of 1.11 $\mu mol\cdot L^{-1}$ for phorate. Zhang et al. [36] optimized the aptamer sequence specific to phorate and established a fluorescence detection method grounded on the competition between the molecular beacon and the aptamer for quantitative phorate detection. Researchers have also integrated Apt with various techniques such as surface-enhanced Raman scattering [37], colorimetry [38,39], capillary electrophoresis [40], sensor methods [41], and fluorescence assays [42,43] to detect phorate, achieving remarkable performance.

In this work, we prepared a novel type of aptamer-functionalized MNPs specific to phorate. By using the superparamagnetic properties and biocompatibility of MNPs, as well as the strong specificity and adsorption ability of the aptamer for phorate, we developed an MSPE method for enriching and extracting phorate from plasma samples, followed by GC-MS analysis. We characterized the prepared magnetic materials through various methods and optimized extraction and elution conditions. In addition, we evaluated the extraction performance of phorate in plasma samples.

2 Experiments

2.1 Chemicals and reagents

We procured four methanol-soluble standard solutions, including phorate, parathion, chlorpyrifos, and methyl parathion, from the Chinese Academy of Metrology, each possessing a concentration of 1 $mg\cdot mL^{-1}$. The aptamer sequence employed was 5′- AAGCTTTTATATATGCGCAGCGATTTTGAT CGAAAGGCTGAGAGCTACGC-3′, featuring NH_2 modification at its 5′ terminus, and it was synthesized by Bioengineering Shanghai Co., Ltd. Other chemicals and reagents, such as $FeCl_3\cdot 6H_2O$, ethylene glycol, sodium acetate, tetraethoxysilane (TEOS), 3-aminopropyltriethoxysilane (APTES), succinic anhydride, and 2-(*N*-morpholino)ethanesulfonic acid (MES), were procured from Shanghai Aladdin Biochemical Technology Co., Ltd. In addition, ammonia, toluene, and *N*,*N*-dimethylformamide (DMF) were sourced from Tianjin Oubokai Chemical Co., Ltd. 1-Ethyl-(3-dimethylaminopropyl)carbodiimide (EDC), *N*-hydroxysuccinimide (NHS), tris(hydroxymethyl)aminomethane (Tris), and bovine serum albumin (BSA) were obtained from Bioengineering Shanghai Co., Ltd. Solvents employed, such as methanol, acetonitrile, ethanol, acetone, ethyl acetate, and dichloromethane, were acquired from Honeywell Trading Shanghai Co., Ltd. Purified water, characterized by a resistance of 18.2 MΩ, was generated in-house employing a Millipore pure water system.

2.2 Instrumentations

The morphology and dimensions of MNPs were ascertained through scanning electron microscopy (SEM) (Zeiss Merlin Compact) and transmission electron microscopy (TEM) (Jeol JEM 2100). Infrared spectra were acquired utilizing a Fourier-transform infrared spectrometer (FTIR) (Thermo Scientific Nicolet iS20). The ξ potential was determined through dynamic light scattering (DLS) (Malvern Zetasizer

Nano ZS90). The hysteresis curve of MNPs was measured via a vibrating sample magnetometer (VSM) (LakeShore 7404). Additional instruments employed included a pH meter (METTLER TOLEDO FE20), a constant temperature culture oscillator (ZHICHENG ZWY-200D), and a confocal laser scanning microscope (CLSM) (Olympus FV1200).

For analytical purposes, gas chromatography-mass spectrometry (GCMS-QP2020 NX, SHIMADZU) was utilized and coupled with a chromatographic column (SH-Rxi-5Sil MS; 30 m × 0.25 mm; 0.25 μm). The chromatographic conditions featured helium as the carrier gas, a split injection method (10:1), and a column flow rate of 1 mL·min^{-1}. The temperature program for the chromatographic column included an initial temperature of 100°C for 2 min, followed by a ramp to 280°C at a rate of 20°C·min^{-1}, and succeeded by an 8 min hold at 280°C. The sample inlet and transmission line temperatures were set at 280°C and 260°C, respectively. Electron bombardment ionization (EI) was employed, with an EI energy of 70 eV and an ion source temperature of 250°C. Selective ion scanning mode was employed to detect characteristic fragment ions of phorate, including 75, 121, and 231.

2.3 Preparation of aptamer-functionalized MNPs

We synthesized core-shell aptamer-functionalized MNPs specific to phorate through a sequential process involving the solvothermal method and the self-assembly method, as delineated in Figure 1.

Synthesis of Fe_3O_4 MNPs via the solvothermal method [44]: Initially, 5.4 g of $FeCl_3{\cdot}6H_2O$ was entirely dissolved in 80 mL of ethylene glycol. Subsequently, 7.2 g of sodium acetate was added with continuous stirring until homogeneity was achieved. This mixture was subsequently placed into the reactor and subjected to a 10 h reaction at 200°C, followed by natural cooling to room temperature. The resulting product was magnetically separated, purified, and subjected to vacuum drying to obtain Fe_3O_4·MNPs.

Synthesis of Fe_3O_4@SiO_2 MNPs [45]: In the first step, 1 g of Fe_3O_4 MNPs was introduced into a mixture comprising 150 mL of anhydrous ethanol and 50 mL of water, followed by stirring to attain a uniform mixture. Next, 5 mL of ammonia was added, and after 15 min of reaction time, 50 mL of TEOS ethanol solution (1:50) was added dropwise with continuous stirring for 8 h. The resulting product was then magnetically separated, washed, and activated using 1 mol·L^{-1} hydrochloric acid. Subsequently, it was rinsed and vacuum dried to yield Fe_3O_4@SiO_2 MNPs.

Amination and carboxylation of Fe_3O_4@SiO_2 MNPs: Initially, 0.5 g of Fe_3O_4@SiO_2 MNPs was thoroughly mixed with 5 mL of APTES and 45 mL of toluene. The reaction was conducted at 60°C for 10 h with stirring under a nitrogen atmosphere. Following the reaction, the product was magnetically separated, rinsed with ethanol, and subjected to vacuum drying to yield Fe_3O_4@SiO_2-NH_2 MNPs. Subsequently, an additional 0.2 g of Fe_3O_4@SiO_2-NH_2 MNPs and 8 g of succinic anhydride were combined with 150 mL of anhydrous DMF, followed by ultrasonic dispersion and continuous stirring. The reaction was stirred at 60°C for 12 h under a nitrogen atmosphere. After the reaction, the product was magnetically

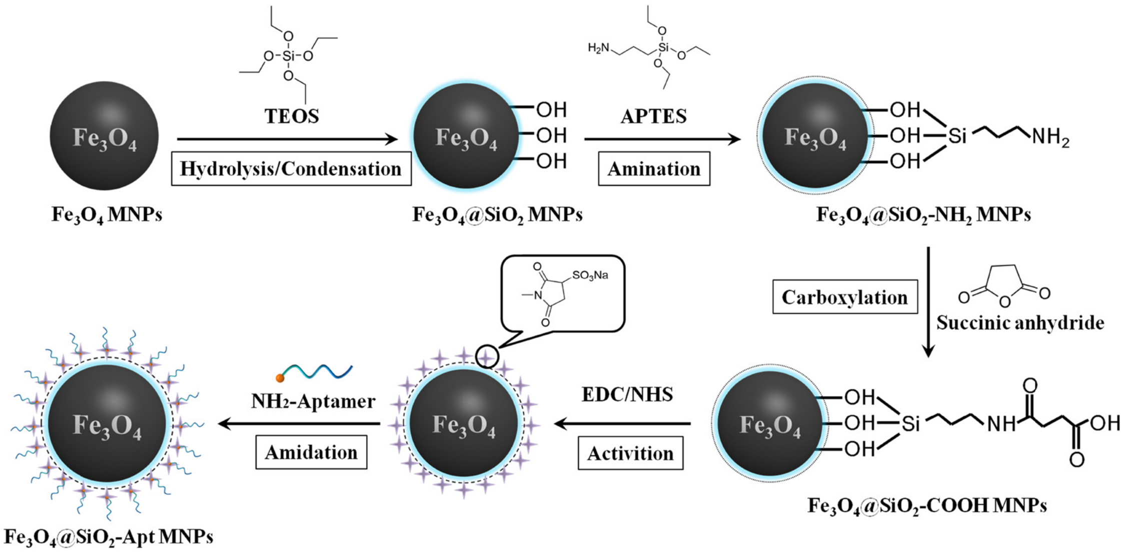

Figure 1: Schematic preparation of the aptamer-functionalized MNPs.

separated, washed with DMF and water, and subjected to vacuum drying to obtain Fe_3O_4@SiO_2-COOH MNPs.

Synthesis of aptamer-functionalized MNPs (Fe_3O_4@SiO_2-Apt): Initially, 1 mg of Fe_3O_4@SiO_2-COOH MNPs was dispersed in a MES buffer solution (0.025 mol·L^{-1}, pH 5.5). The carboxyl group was activated using freshly prepared EDC and NHS (50 µL each at 50 mg·mL^{-1}). The activated MNPs were then magnetically separated, rinsed, and subjected to the addition of 0.5 nmol Apt-NH_2. This mixture was incubated with slow oscillation at 37°C for 6 h. The unreacted active carboxylic acid components were removed using Tris-HCl buffer (0.05 mol·L^{-1}, pH 8.0). After further washing, 1% BSA was introduced to minimize nonspecific adsorption sites on the MNPs' surface. Finally, the Fe_3O_4@SiO_2-Apt MNPs were obtained through repeated washing.

2.4 Adsorption experiments

The binding capacity of Fe_3O_4@SiO_2-Apt MNPs to the target was investigated through multiple adsorption experiments.

Adsorption kinetics study: 50 mg of Fe_3O_4@SiO_2-Apt MNPs were introduced into a 5 mL sample solution with a concentration of 200 ng·mL^{-1} (pH = 7.0). Following dispersion and thorough mixing, the sample solution was placed into a thermostatic oscillator and incubated at 25°C with a rotating rate of 200 rpm for varying durations (2, 4, 6, 8, 10, 12, 14, 16, 18, and 20 min). After the completion of adsorption, the adsorbent was separated magnetically by an external strong magnet, and the supernatant was collected.

Adsorption isotherm measurement: 50 mg of Fe_3O_4@SiO_2-Apt MNPs were added to 5 mL sample solutions with different concentrations (50–1,200 ng·mL^{-1}) for dispersion. Following dispersion and thorough mixing, the sample solution was placed into a thermostatic oscillator and incubated at 25°C with a rotating rate of 200 rpm for 10 min. Subsequent to adsorption completion, the adsorbent was separated magnetically by an external strong magnet, and the supernatant was collected.

2.5 Preparation of the standard solution and the sample solution

A 1 mg·mL^{-1} phorate standard solution in methanol was employed for this study. Standard solutions were prepared

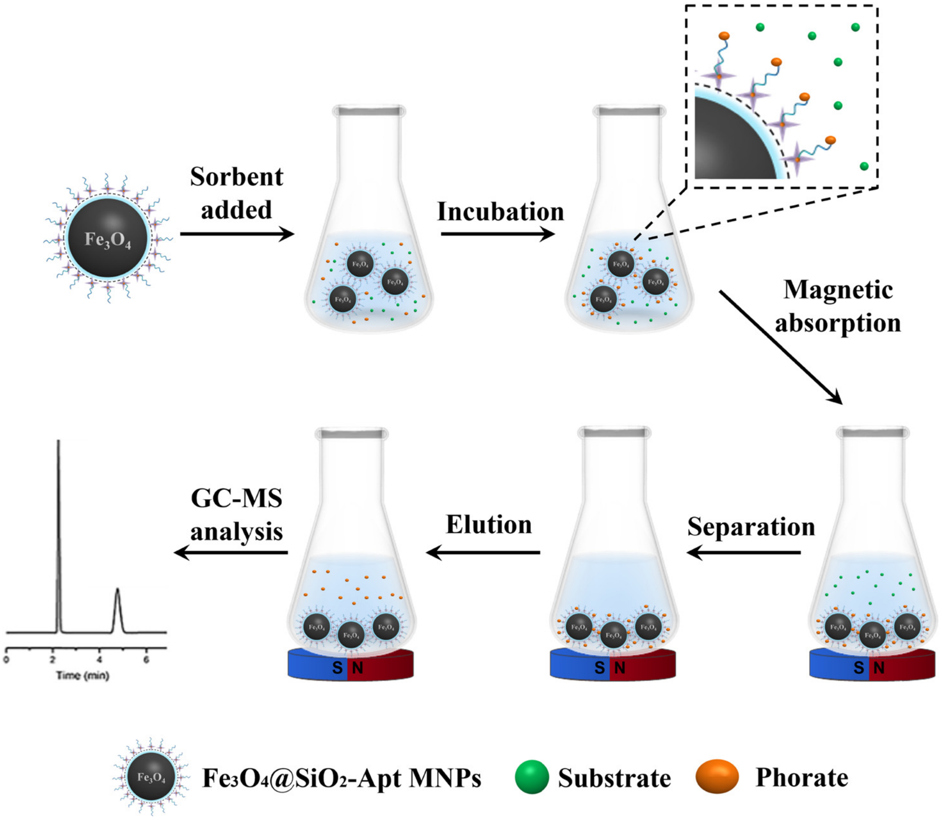

Figure 2: Schematic extraction procedure of phorate by Fe_3O_4@SiO_2-Apt MNPs.

through stepwise dilution with methanol and stored at 4°C with a 1-month shelf life. Blank human plasma samples were obtained from the Zhangjiakou Blood Center. For the experiments, plasma samples were diluted with ultrapure water at a 1:4 ratio, and the pH was adjusted to 8.0 by the addition of an appropriate quantity of 0.1 $mol \cdot L^{-1}$ NaOH. After vortexing for 5 min, followed by centrifugation at 8,000 rpm for 5 min, the supernatant was collected as the experimental sample for subsequent extraction.

2.6 Magnetic dispersive solid-phase extraction process

Figure 2 depicts the extraction process of phorate from plasma samples utilizing Fe_3O_4@SiO_2-Apt MNPs. A 5 mL plasma sample containing phorate was acquired, and the sample's pH was adjusted to 7.0. To attain a salt concentration of 4% (w/v), NaCl was introduced. Subsequently, 50 mg of Fe_3O_4@SiO_2-Apt MNPs were added to the sample and thoroughly mixed. The mixture was subsequently incubated at 25°C with continuous agitation at 200 rpm for 10 min in a constant temperature culture oscillator. During this incubation, phorate bound to the aptamer and adsorbed onto the MNPs. Following the incubation, MNPs were concentrated at the bottom of the container, employing an external magnetic field. The supernatant was meticulously removed, and the MNPs underwent multiple washes to eliminate nonspecific adsorbents. Next, 1.2 mL of the ethyl acetate eluate was introduced to the MNPs. Following vortexing and oscillation for 5 min, the phorate bound to the MNPs was successfully eluted. The eluate was carefully collected, slowly dried under a nitrogen stream, and subsequently re-dissolved in 200 μL of methanol for further phorate detection via GC-MS.

3 Results and discussion

3.1 Structure and adsorption mechanism of material

The nanosized Fe_3O_4 grains were synthesized using the solvothermal method and served as the core for the core-shell material. Subsequently, the SiO_2 sol was continuously generated through the hydrolysis condensation effect of TEOS. In this process, the surface of Fe_3O_4 became positively charged, while SiO_2 acquired a negative charge, enabling SiO_2 to directly adhere to the surface of Fe_3O_4 particles. After further growth, the Fe_3O_4@SiO_2 composite material was formed. At this juncture, the material's surface was enriched with hydroxyl groups, facilitating further modification and enhancing stability, hydrophilicity, and biocompatibility. Following amination and carboxylation reactions, a substantial number of carboxyl groups were attached to the material's surface. Subsequently, the EDC/NHS coupling reagent was added to connect the amine-modified aptamer to the material's surface, ultimately yielding Fe_3O_4@SiO_2-Apt. This material, which can capture phorate through its aptamer, underwent denaturation and annealing at 90°C to induce the randomly coiled aptamer to form a stem-ring secondary structure. This structure includes specific binding sites, enabling the aptamer to bind to phorate molecules in a highly specific and affinity-driven manner through potential molecular shape complementarity, van der Waals forces, and hydrogen bonding, thereby achieving phorate adsorption by the material.

3.2 Characterization of aptamer-functionalized MNPs

The morphology, particle size, and dispersion of Fe_3O_4 MNPs were analyzed using SEM, and the characterization results are presented in Figure 3(a). Fe_3O_4 MNPs exhibited a spherical shape with a particle size of approximately 300 nm. The particle size distribution was relatively uniform, and the dispersion was excellent. Furthermore, a comparison of the characterization between single particles of Fe_3O_4 MNPs and Fe_3O_4@SiO_2 MNPs using TEM is displayed in Figure 3(b) and (c). In this comparison, it is evident that Fe_3O_4@SiO_2 MNPs were uniformly coated with a SiO_2 layer, approximately 20 nm thick, forming a core-shell structure. This SiO_2 coating effectively reduced their surface energy and enhanced their stability. In addition, the hydrophilic hydroxyl groups added to the MNPs' surface improved their hydrophilicity, enabling better dispersion in aqueous solutions [46].

Subsequently, FTIR spectroscopy was employed to characterize the functional groups present on the surfaces of Fe_3O_4 MNPs, Fe_3O_4@SiO_2 MNPs, Fe_3O_4@SiO_2-NH_2 MNPs, and Fe_3O_4@SiO_2-COOH MNPs, and the obtained results are presented in Figure 4. Notably, a distinctive stretching vibration peak corresponding to the Fe–O bond was observed at 580 cm^{-1} in the MNPs. Peaks at 1,085, 796, and 462 cm^{-1} were associated with the Si–O–Si antisymmetric stretching vibration and symmetric vibration. A stretching vibration peak characteristic of Si–OH appeared at 944 cm^{-1}, indicating the presence of a SiO_2 coating on the outer surface of the MNPs. On the surface of Fe_3O_4@SiO_2-NH_2 MNPs, peaks at 1,024, 1,577, and 640 cm^{-1} were indicative of the C–N stretching vibration, in-plane N–H bending vibration, and out-of-plane

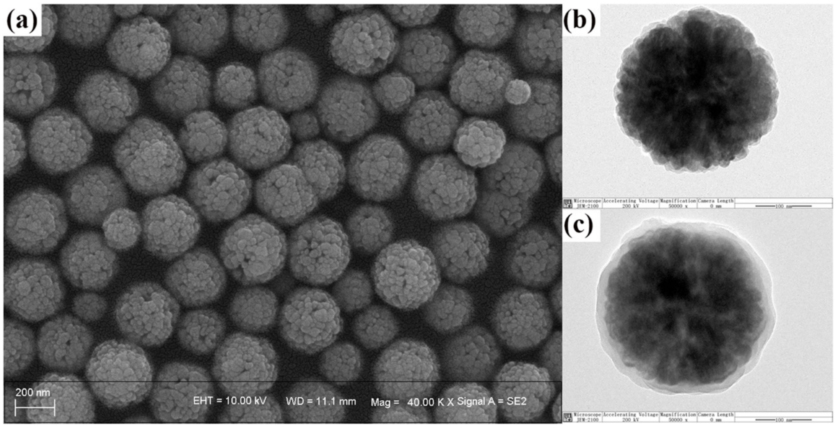

Figure 3: (a) SEM image of Fe_3O_4 MNPs, (b) TEM image of Fe_3O_4 MNPs, and (c) TEM image of $Fe_3O_4@SiO_2$ MNPs.

N–H bending vibration, respectively. These three peaks indicated the successful completion of amine modification on the MNPs. For $Fe_3O_4@SiO_2$-COOH MNPs, the characteristic C═O absorption peak at 1,584 cm^{-1} was significantly enhanced. In addition, peaks at 1,380 and 1,400 cm^{-1} corresponded to the C–O symmetric vibration and O–H in-plane bending vibration in carboxylic acid, respectively, indicating the successful modification of carboxyl groups on the MNPs' surface. Furthermore, we utilized DLS to measure the ξ potential of $Fe_3O_4@SiO_2$ MNPs, $Fe_3O_4@SiO_2$-NH_2 MNPs, and $Fe_3O_4@SiO_2$-COOH MNPs, revealing ξ potentials of approximately −26.79 ± 1.31, −18.05 ± 1.77, and 29.72 ± 0.93 mV, respectively. These results further substantiated the successful sequential modification of amino and carboxyl groups on the surface of the MNPs.

Additional surface information was derived from the X-ray photoelectron spectroscopy (XPS) analysis, and the variations in surface atomic content of the MNPs were quantified based on the measured XPS transitions (Table 1). This analysis demonstrated the sequential modification of functional groups on the MNPs. The wide scan XPS spectra (Figure 5(a)) exhibited peaks at 102.9, 154.4, 284.62, 399.61, 532.26, and 710.56 eV, corresponding to Si 2p, Si 2s, C 1s, N 1s, O 1s, and Fe 2p, respectively. In the Si 2p spectrum (Figure 5(e)), the presence of the Si–O bond at 102.9 eV in $Fe_3O_4@SiO_2$-COOH MNPs was evident. Figure 5(b) displays characteristic peaks at 710.5 and 724.3 eV for Fe 2p3/2 and Fe 2p1/2, respectively, indicating the coexistence of multiple oxidation states of Fe in the Fe_3O_4. Carbon bonds were deconvoluted into C–C (284.3 eV), C–O (285.2 eV), and C═O (288.1 eV) (Figure 5(c)), while oxygen bonds were deconvoluted into C═O (529.9 eV) and C–OH (532.3 eV) (Figure 5(d)). These results further confirmed the successful attachment of carboxyl groups to the surface of Fe_3O_4 MNPs. The modification with carboxyl groups provided stable binding sites for the amino-modified Apt through a condensation reaction between carboxyl and amino groups. In addition, the surface-modified carboxyl groups (hydrophilic groups) enhanced the hydrophilicity and dispersibility of the MNPs.

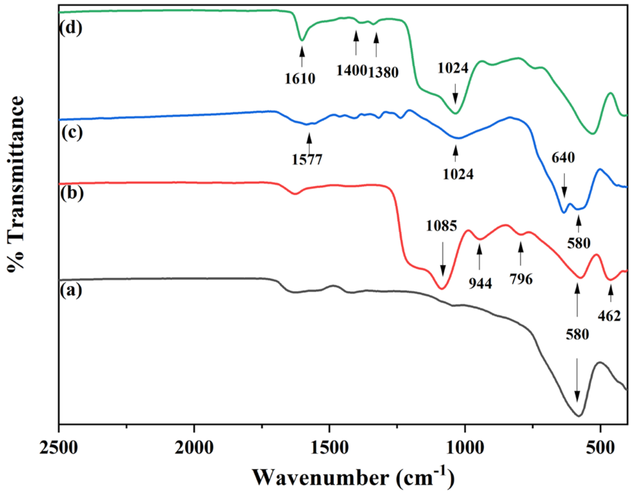

Figure 4: FTIR spectra of (a) Fe_3O_4, (b) $Fe_3O_4@SiO_2$, (c) $Fe_3O_4@SiO_2$-NH_2, and (d) $Fe_3O_4@SiO_2$-COOH MNPs.

To confirm the successful modification of the aptamer on the MNPs' surface, the 3′ end of the aptamer was labeled

Table 1: Comparison of element content on the surface of MNPs resulting from the XPS spectra

Compound	Atomic %				
	C 1s	O 1s	Si 2p	N 1s	Fe 2p
Fe_3O_4 MNPs	25.56	45.82	2.11	0.42	26.09
$Fe_3O_4@SiO_2$ MNPs	32.5	44.75	19.66	0.44	2.65
$Fe_3O_4@SiO_2$ and the variations in surface NH_2 MNPs	38.35	34.65	17.99	7.87	1.14
$Fe_3O_4@SiO_2$ and the variations in surface COOH MNPs	24.52	52.81	16.95	2.55	3.17

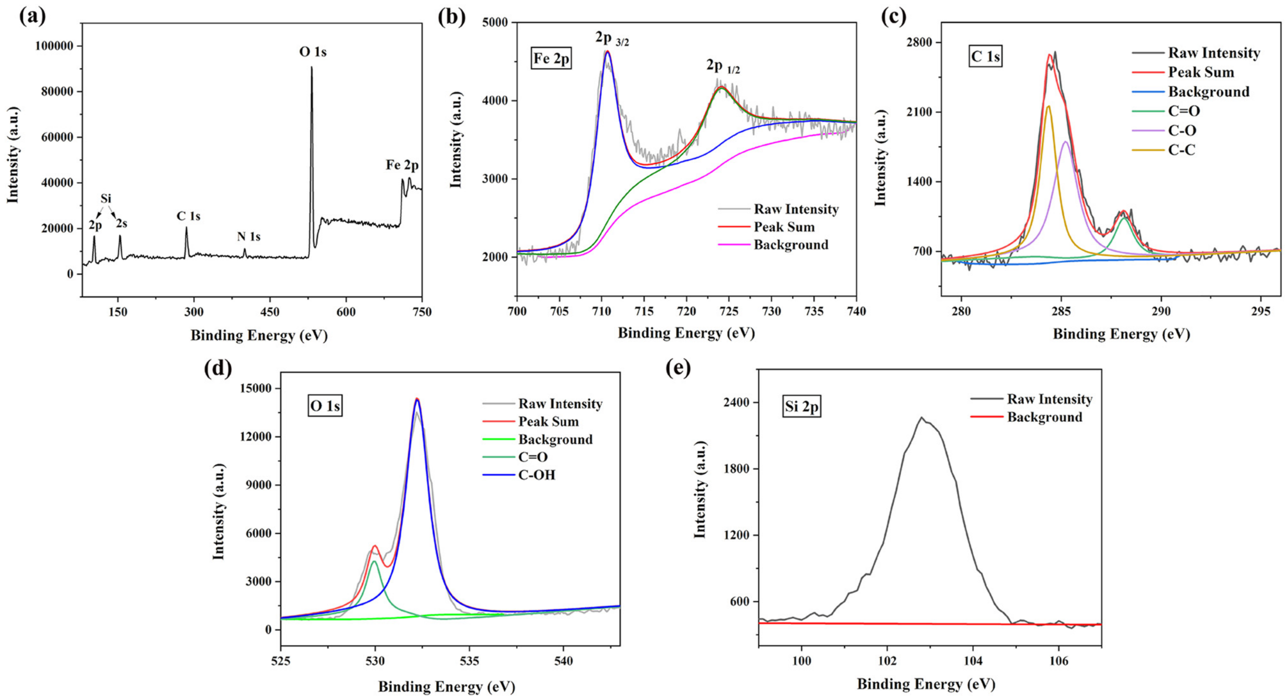

Figure 5: (a) Survey XPS spectra of $Fe_3O_4@SiO_2$-COOH MNPs; deconvoluted high-resolution XPS spectra of (b) Fe 2p, (c) C 1s, (d) O 1s, and (e) Si 2p of $Fe_3O_4@SiO_2$-COOH MNPs.

with a fluorescent dye (6-carboxyfluorescein, 6-FAM), and $Fe_3O_4@SiO_2$-Apt (6-FAM) MNPs were characterized using CLSM. The results shown in Figure 6 showed green fluorescence in the dark field of the CLSM when excited at 488 nm. The green fluorescence corresponded to the position of the MNPs in both the bright field and the combined field of views, confirming that the green fluorescence emanated from the surface of the MNPs. This affirmed the successful modification of the aptamer specific to phorate on the MNPs' surface.

To evaluate the saturation magnetization of the sorbent, VSM was employed. The magnetization saturation values (Ms) for Fe_3O_4 MNPs, $Fe_3O_4@SiO_2$ MNPs, and $Fe_3O_4@SiO_2$-Apt MNPs were determined to be 83.63, 72.41, and 63.86 emu·g^{-1}, respectively (Figure 7). The reduction in Ms value for $Fe_3O_4@SiO_2$-Apt MNPs, compared to Fe_3O_4 MNPs, could be attributed to the presence of nonmagnetic materials such as SiO_2, APTES, and the aptamer on the MNPs' surface. Nevertheless, $Fe_3O_4@SiO_2$-Apt MNPs still exhibited superparamagnetism and maintained sufficient magnetic

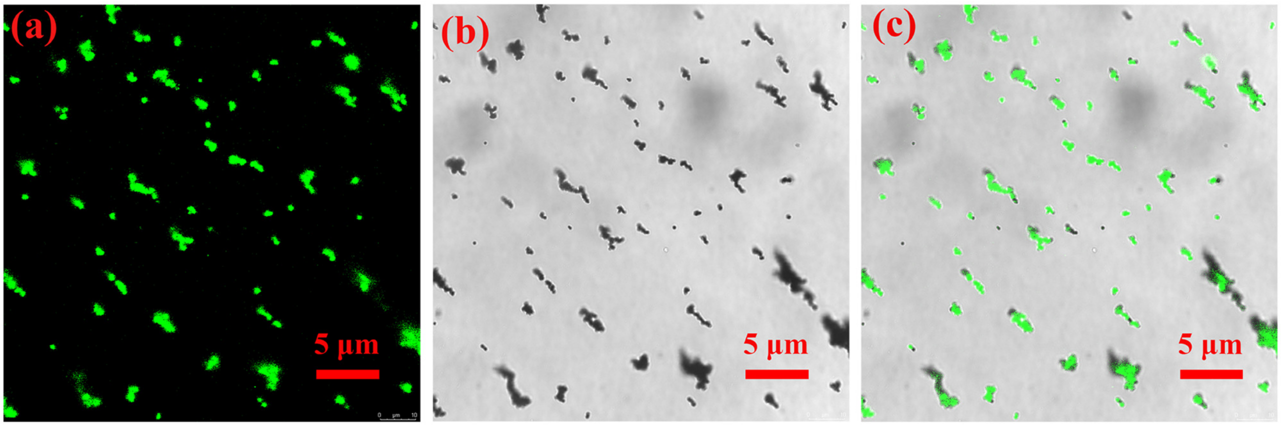

Figure 6: CLSM images of $Fe_3O_4@SiO_2$-Apt (6-FAM) MNPs in (a) dark field, (b) bright field, and (c) merge channels.

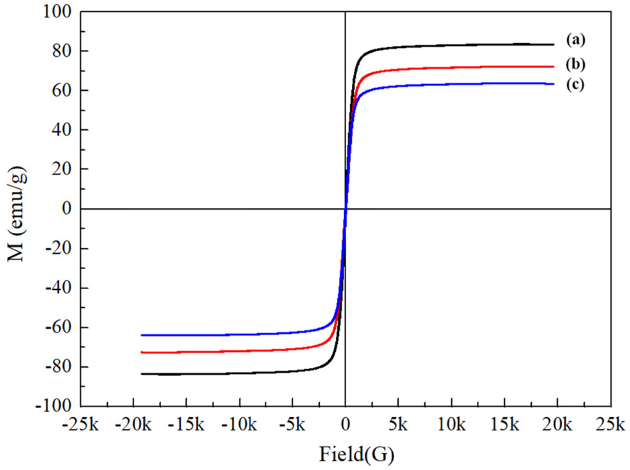

Figure 7: Magnetization curves of (a) Fe_3O_4 MNPs, (b) $Fe_3O_4@SiO_2$ MNPs, and (c) $Fe_3O_4@SiO_2$-Apt MNPs.

response strength for effective magnetic separation, facilitating the reuse of the sorbent.

3.3 Optimization of the extraction conditions

To enhance the extraction of phorate from the sample using $Fe_3O_4@SiO_2$-Apt MNPs, we conducted optimization of various extraction conditions employing a single-factor approach. These conditions included the binding mode, extraction time, solution pH, ionic strength, and the amount of sorbent. A sample solution with a phorate concentration of 200 ng·mL^{-1} was employed as the target for this research.

3.3.1 Binding mode

We explored various binding methods to enhance the phorate-capturing process by $Fe_3O_4@SiO_2$-Apt MNPs, which could impact the extraction efficiency. Three methods were investigated: ultrasonication, vortexing, and incubation. The results showed that the incubation method produced higher recovery rates under the same conditions. This was because gentle oscillation promoted the dispersion of MNPs, facilitating the binding of the target to the adsorption site. In contrast, high-frequency oscillation generated by ultrasonication and vortexing had the potential to somewhat damage the surface modifiers of MNPs, affecting the integrity of the aptamer. In addition, we examined the effects of incubation temperature and rotation speed, with the highest recovery rate (90%) observed at a temperature of 25°C and a rotation speed of 200 rpm.

3.3.2 Extraction time

The MSPE method relied on achieving adsorption equilibrium between $Fe_3O_4@SiO_2$-Apt MNPs and phorate. Extending the extraction time was beneficial for ensuring full contact between the aptamer and the target, thus ensuring high extraction efficiency. We studied the binding rate of phorate captured by $Fe_3O_4@SiO_2$-Apt MNPs within the 2–20 min range. As shown in Figure 8(b), as the extraction time increased, the recovery rate displayed an upward trend and essentially stabilized at 10 min, indicating that adsorption had reached equilibrium. In the early stage of the adsorption process, a large number of active sites were provided by the stem-ring structure of Apt on the material's surface, resulting in a rapid adsorption rate and a significant increase in adsorption in a short time. As the adsorption process continued, the target molecules on the material's surface increased, enhancing intermolecular repulsive forces and leading to occupied adsorption sites, thus slowing down the adsorption rate until it stabilized. Therefore, we selected 10 min as the optimal extraction time.

3.3.3 pH of the solution

The pH values of the solution affected the surface charge of the sorbent and the folding configuration of the aptamer, consequently influencing the extraction efficiency of phorate by the sorbent. In addition, phorate was susceptible to hydrolysis in strongly acidic or alkaline environments, making extraction unfeasible. Considering these factors, we experimentally studied extraction efficiency within the pH range of 5–8, adjusting the pH using 0.1 mol·L^{-1} HCl or NaOH solution. The recovery rates at different pH values are presented in Figure 8(c). The results indicated that extraction under neutral conditions was superior to extraction under acidic and alkaline conditions. The reason is that the isoelectric point of the nucleic acid aptamer is less than 7, and under neutral conditions, it is negatively charged, resulting in a certain electrostatic repulsion and the ability to maintain the stem-ring structure stably, providing active sites for better binding with phorate. Therefore, we selected pH 7.0 as the optimal experimental condition.

3.3.4 Ionic strength

A certain concentration of Na^+ in the solution enhanced the stability of the aptamer's structure. Furthermore, an increase in ionic strength reduced the solubility of the target substance, thereby improving extraction efficiency. We investigated extraction efficiency within the concentration range of 0–10% (w/v) by adding NaCl to the reaction solution. The results are illustrated in Figure 8(d). With the increasing NaCl concentration, there was a corresponding increase in the recovery rate. At a 4% (w/v) concentration, the recovery rate reached 94%. Moreover, a further increase in NaCl concentration resulted in a decreased recovery rate due to increased solution viscosity, which in turn led to reduced molecular mass transfer rates, thereby impeding the binding between the phorate and the aptamer. Considering the influence of Na^+ on the electronegativity of the aptamer, an excess of Na^+ ions would neutralize the negative charge on the aptamer molecule and weaken the electrostatic repulsion between Apt, potentially facilitating polymerization, which could affect stability. Consequently, we opted for 4% (w/v) NaCl as the optimal ionic strength for subsequent experiments.

3.3.5 Amount of sorbent

The quantity of sorbent directly exerts influence upon the number of available aptamer binding sites, a pivotal factor in enhancing extraction efficiency. We explored sorbent quantities ranging from 10 to 80 mg. As illustrated in Figure 8(e), the recovery rate reached its zenith and remained relatively stable when the sorbent amount reached 50 mg. Therefore, we opted for 50 mg as the optimal sorbent quantity for subsequent experiments.

3.4 Optimization of elution conditions

During the experiment, altering the water-organic environment could reversibly change the three-dimensional oligonucleotide structure of the aptamer on the sorbent's surface. This modification affected the interaction between the aptamer and phorate, enabling phorate elution. To enhance target elution, we optimized pertinent elution conditions, including the choice of elution solvent, elution solvent volume, and elution time.

3.4.1 Selection of elution solvent

We scrutinized the elution characteristics of six solvents with varying polarities: acetonitrile, methanol, ethanol,

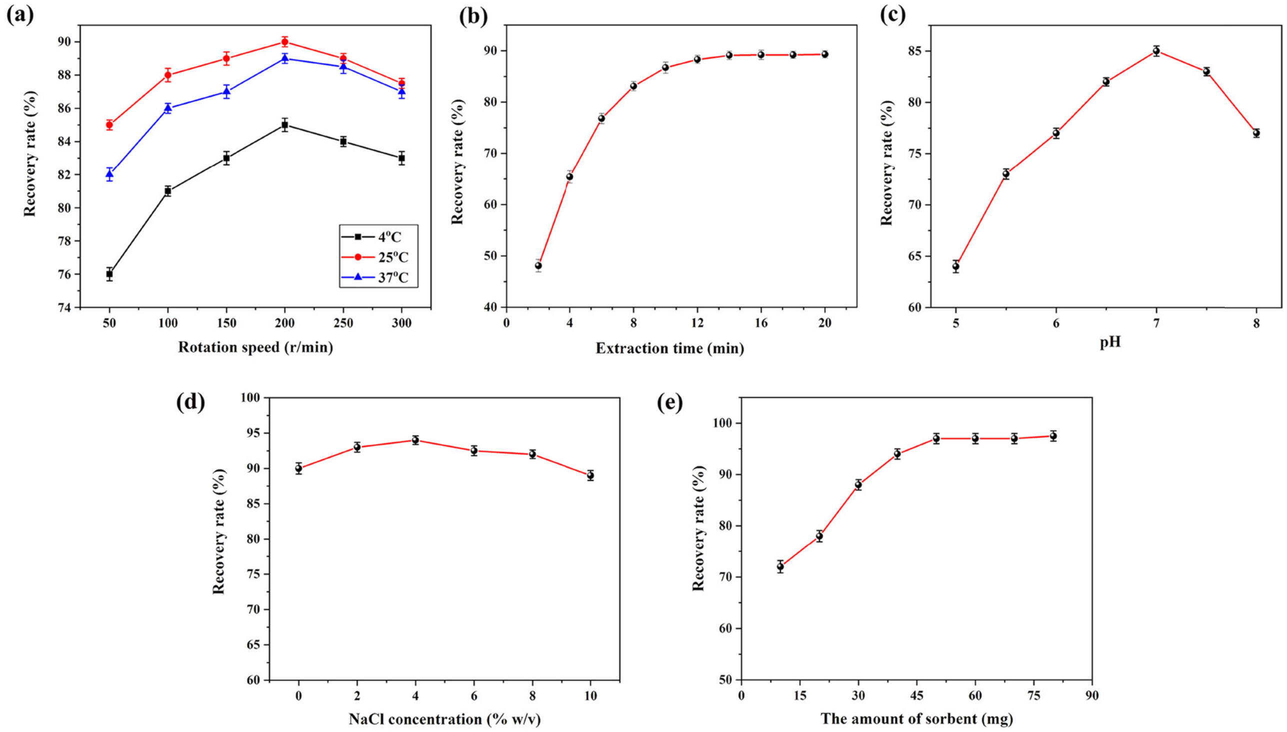

Figure 8: Effects of extraction conditions on the recovery rate for phorate: (a) rotation speed, (b) extraction time, (c) pH of solution, (d) NaCl concentration, and (e) the amount of sorbent.

acetone, ethyl acetate, and dichloromethane. As portrayed in Figure 9(a), ethyl acetate and dichloromethane exhibited superior elution efficiency. This outcome aligns with the relatively low polarity of phorate. Following the principle of like-dissolves-like, phorate exhibited greater solubility in ethyl acetate and dichloromethane due to their lower polarity. Taking into consideration the toxicity, volatility, and reusability of these two solvents, we chose ethyl acetate as the elution solvent for subsequent experiments.

3.4.2 Volume of the elution solvent

Sufficient elution solvent ensures the extraction of more target substances, enhancing extraction efficiency. Simultaneously, selecting the smallest elution solvent volume enhances the method's EF. The recovery rate of phorate was assessed using ethyl acetate as the elution solvent within the range of 0.2–2 mL, and the results are depicted in Figure 9(b). With an increase in elution solvent volume, the recovery rate gradually rose. When the volume reached 1.2 mL, the rate of increase in recovery became less pronounced. Thus, considering the minimum solvent volume feasible, we ultimately selected 1.2 mL as the elution solvent volume.

3.4.3 Elution time

We experimentally probed the impact of elution time on extraction efficiency. The experimental outcomes are illustrated in Figure 9(c). As elution time increased, the recovery rate gradually reached equilibrium after 5 min. Extending the elution time to 10 min did not lead to a noticeable change in the recovery rate. In light of these results, 5 min was chosen as the optimal elution time.

3.5 Adsorption isotherms and kinetic experiments

To investigate the adsorption process of $Fe_3O_4@SiO_2$-Apt MNPs on phorate, we employed a pseudo-first-order kinetic model and a pseudo-second-order kinetic model to analyze the experimental data, as expressed in equations:

$$\ln(Q_e - Q_t) = \ln Q_e - k_1 \cdot t \tag{1}$$

$$\frac{t}{Q_t} = \frac{1}{k_2 \cdot Q_e^2} + \frac{t}{Q_e} \tag{2}$$

where t represents the adsorption time, and Q_e and Q_t are the adsorption amounts of phorate at equilibrium and any time, respectively. k_1 and k_2 denote the equilibrium rate constant of the pseudo-first-order and pseudo-second-order kinetic models, respectively.

The calculated parameters of the relevant dynamic models are presented in Table 2. As observed in Table 2, R^2 and Q_e values obtained by fitting the pseudo-first-order kinetic model are 0.9945 and 22.28 ng·mL^{-1}, respectively, whereas those obtained by fitting the pseudo-second-order kinetic model are 0.9994 and 19.53 ng·mL^{-1}. These results indicate that R^2 obtained by fitting Eq. 2 is higher than that obtained by fitting Eq. 1, and the theoretical equilibrium adsorption capacity derived from the pseudo-second-order kinetic

Table 2: Kinetic parameters for phorate adsorption on $Fe_3O_4@SiO_2$-Apt MNPs

Model	**Parameters**	R^2
Pseudo-first order	$k_1 = -0.3535\ \text{min}^{-1}$ $Q_e = 22.28\ \text{ng}\cdot\text{mg}^{-1}$	0.9945
Pseudo-second order	$k_2 = 0.02168\ \text{min}^{-1}$ $Q_e = 19.53\ \text{ng}\cdot\text{mg}^{-1}$	0.9994

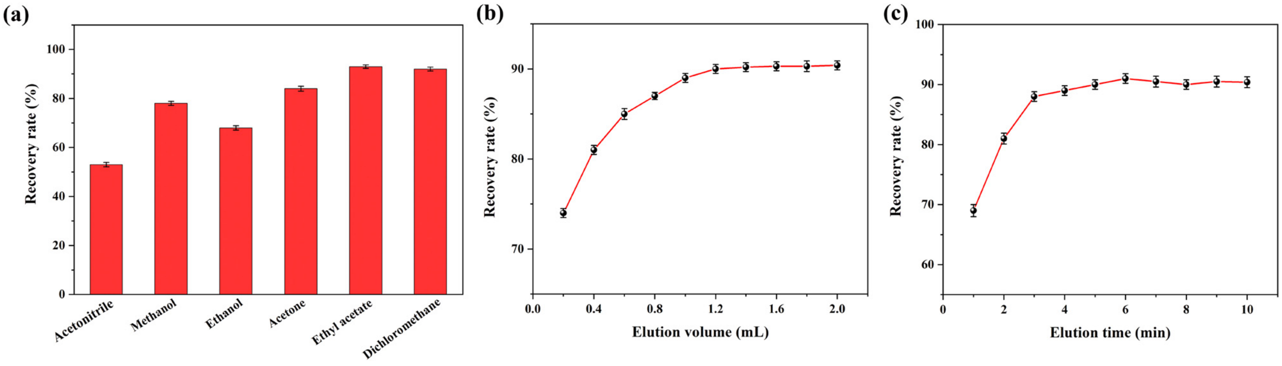

Figure 9: Effects of elution conditions on the recovery rate for phorate: (a) elution solvents, (b) volume of the elution solvent, and (c) elution time.

Table 3: Parameters of the Langmuir and Freundlich isotherm models for phorate adsorption in $Fe_3O_4@SiO_2$-Apt MNPs

Adsorption isotherm model	Parameters
Lagmuir	Q_{max} = 78.54 ng·mg^{-1} k_L = 0.0472 mL·mg^{-1} R^2 = 0.9978
Freundlich	k_F = 15.0581 mL·mg^{-1} n = 3.98 R^2 = 0.8776

equation is closer to the experimental value (19.07 ng·mg^{-1}). This suggests that the adsorption process of $Fe_3O_4@SiO_2$-Apt MNPs to phorate aligns more closely with the pseudo-second-order kinetic model (Kinetic adsorption curve and pseudo-second-order model fitting curve are shown in Figure 10). This indicates that the adsorption rate of phorate is controlled by a chemical mechanism, possibly due to hydrogen bonding or van der Waals interactions between the active sites generated by the stem-ring structure of the aptamer and the phorate molecule.

To further investigate the adsorption process of $Fe_3O_4@SiO_2$-Apt MNPs on phorate, we utilized the Langmuir and Freundlich isothermal models to evaluate the adsorption performance of $Fe_3O_4@SiO_2$-Apt MNPs.

$$\frac{C_e}{Q_e} = \frac{1}{Q_{max} \cdot k_L} + \frac{C_e}{Q_{max}} \quad (3)$$

$$\ln Q_e = \ln k_F - \frac{1}{n} \ln C_e \quad (4)$$

Here, C_e represents the concentration of phorate under adsorption equilibrium, Q_e is the adsorption capacity per unit mass of the adsorbent at equilibrium, Q_{max} is the maximum adsorption capacity per unit mass of the adsorbent, K_L is the Langmuir affinity constant, and K_F and n are the Freundlich adsorption equation constants.

The parameters and correlation coefficients for the isotherm models obtained from experimental data are summarized in Table 3. The Langmuir adsorption isothermal model is found to be more suitable than the Freundlich model for the phorate molecule, indicating that the adsorption process is monolayer adsorption. The Q_{max} value calculated by the Langmuir adsorption isothermal model was 78.54 ng·mg^{-1}, which closely matched the experimental value (77.25 ng·mg^{-1}). The adsorption isothermal curve and the Langmuir models fitting curve are shown in Figure 11.

3.6 Method evaluation

Under the optimal extraction conditions, various performance parameters of the method, including the linear range, detection limit, quantitation limit, stability, and others, were experimentally assessed using GC-MS. The results revealed a linear correlation between phorate concentration and chromatographic peak area within the concentration range of 2–700 ng·mL^{-1}, with a linear correlation coefficient (R^2) of 0.9991. The method's detection limit (S/N = 3) was determined to be 0.46 ng·mL^{-1}, and the quantitation limit (S/N = 10) was found to be 1.91 ng·mL^{-1}. Method stability was evaluated through intra-day and inter-day precision. Five parallel experiments were conducted within a single day and over five consecutive days, yielding intra-day and inter-day relative standard deviations (RSDs) of 3.4% and 4.1%, respectively.

3.7 Extraction capacity

The sorbent's specificity was assessed through experimental examination. Five dithiophosphate organophosphate

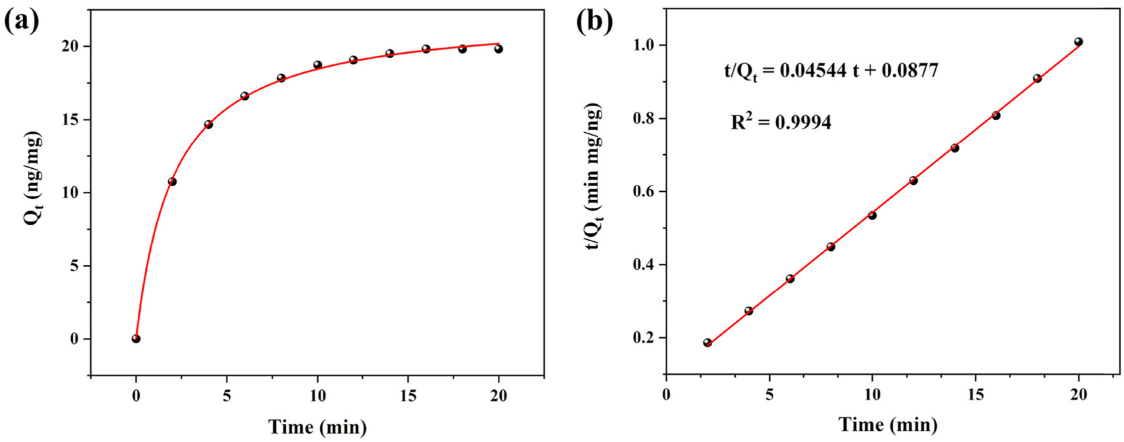

Figure 10: Kinetic adsorption analysis of $Fe_3O_4@SiO_2$-Apt MNPs using phorate as analyte: (a) kinetic adsorption curve and (b) pseudo-second-order model fitting to the experimental values with its linear regression.

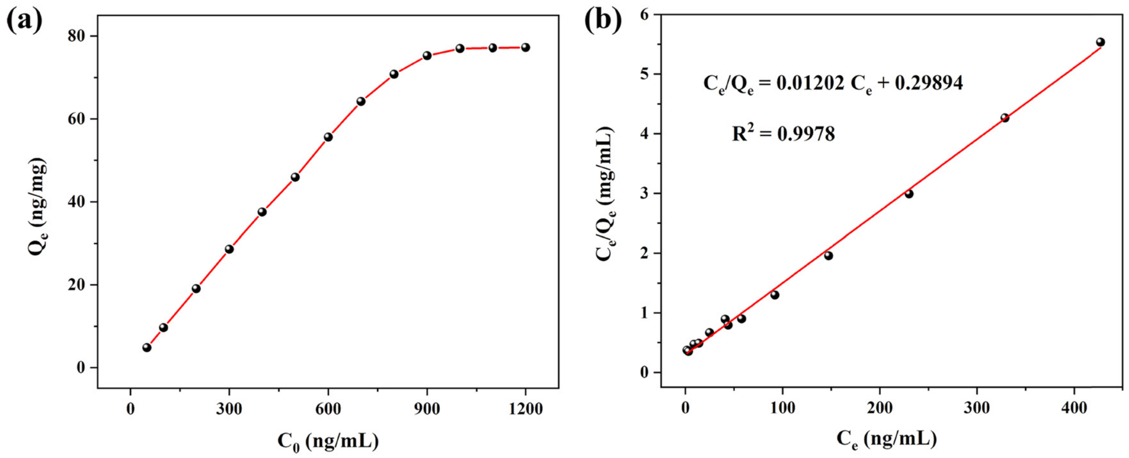

Figure 11: Study of the isothermal adsorption of Fe_3O_4@SiO_2-Apt MNPs using phorate as analyte: (a) adsorption isothermal curve and (b) the Langmuir models fitting the experimental values, with the corresponding linear regressions.

pesticides (terbufos, malathion, dimethoate, ethion, and phosmet) with structures similar to phorate, along with seven common OPPs exhibiting different structures, including phosphate esters (DDVP, moncrotophos), sulfur (ketone)-substituted phosphate esters (phoxim, demeton, parathion, diazinon), and phosphamide esters (methamidophos), were chosen as interfering reagents. These compounds were combined with phorate and introduced into the experimental sample, each at a concentration of 200 $ng\cdot mL^{-1}$. Subsequent to the extraction method, the results are illustrated in Figure 12(a). The recovery of phorate significantly surpassed that of other reagents, indicating the sorbent's strong selectivity for phorate. The nonspecific adsorption of Fe_3O_4 MNPs, Fe_3O_4@SiO_2 MNPs, Fe_3O_4@SiO_2-NH_2 MNPs, and Fe_3O_4@SiO_2-COOH MNPs was investigated, and the results are displayed in Figure 12(b). The recovery rates of phorate by these four MNPs were considerably lower than that of Fe_3O_4@SiO_2-Apt MNPs, indicating minimal nonspecific adsorption by the former.

The sorbent's enrichment capacity was assessed by comparing phorate recovery in different sample volumes. The maximum enrichment volume was determined to be 500 mL, resulting in an EF of 416. In addition, the reusability of the sorbent was investigated, showing that the phorate's recovery rate remained above 80% after 15 successive uses of the sorbent.

3.8 Analysis of real samples

To assess the performance of the adsorption materials in extracting phorate from real plasma samples, the plasma samples underwent pretreatment according to the procedure

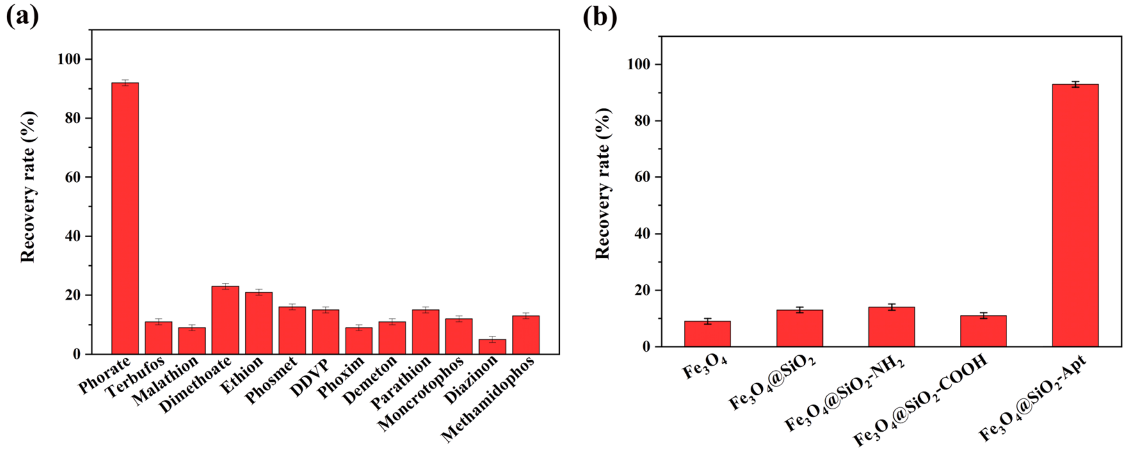

Figure 12: (a) Specificity tests of Fe_3O_4@SiO_2-Apt MNPs and (b) comparison of the extraction efficiency for phorate by the different sorbents.

Table 4: Detection of phorate in plasma samples

Plasma sample	Spiked (ng·mL^{-1})	Found (ng·mL^{-1})	Recovery (%)	RSD (n = 3) (%)
Sample 1	20	17.9	89.5	6.8
	200	203.4	101.7	6.2
	600	589.7	98.3	5.2
Sample 2	20	17.2	86.1	7.7
	200	201.6	100.8	5.9
	600	571.7	95.3	7.3

outlined in Section 2.4. Subsequently, they were subjected to extraction and enrichment following the experimental protocol described in Section 2.5 and analyzed using GC-MS. The results indicated the absence of phorate in the samples. Following this, standard phorate solutions with concentrations of 20, 200, and 600 ng·mL^{-1} were introduced into the plasma sample. The extraction and detection were carried out following the experimental method, and the recoveries of the spiked standards were calculated (n = 3). The experimental results are summarized in Table 4, showing spiked recoveries ranging from 86.1% to 101.7%, with RSDs between 5.2% and 7.7%. These findings affirm the suitability of the method for extracting and detecting phorate in plasma samples. The sources of errors in this study primarily stem from systematic errors. There are numerous manual operations involved in the process of material synthesis and phorate extraction and detection, which can introduce errors. In addition, incomplete or side reactions may occur during the material synthesis process. Therefore, in future research, it is advisable to develop automated methods, increase the number of parallel experiments, and conduct blank and control experiments to minimize the impact of systematic errors on the research.

3.9 Comparison study

The method established in this work was compared with other magnetic solid-phase methods for phorate extraction reported in the literature. The extraction performance and detection parameters are shown in Table 5. As seen from the table, in comparison to other methods, this study exhibits a higher specific recognition ability for phorate and lower cross-reactivity, making it suitable for targeted adsorption detection of phorate in the environment and targeted detection and treatment of individuals poisoned by phorate. In terms of the samples to be detected, this study, using the good hydrophilicity and biocompatibility of the aptamer, explored the extraction of phorate from complex plasma matrices for the first time, demonstrating

Table 5: Comparison of the proposed method with other magnetic methods for determination of phorate

Method	Sorbent	Sample	LOD (ng·mL^{-1})	Linear range (ng·mL^{-1})	Extraction time (min)	Specificity	Reusability	Ref.
MSPE-LC/MS/MS	MVP-DB	Honey	0.1	2–250	20	No	10	[47]
MSPE-GC/FPD	MNPCs	Fruits	1.5 ng·g^{-1}	3–6,000 ng·g^{-}	80	No	—	[25]
R-DSPE- GC/MS/MS	Fe_3O_4@CFR@GO	Chilli	ng·g^{-1}	0.5–100	—	No	5	[48]
MSPE-GC/MS/MS	Fe_3O_4@SiO_2-C18	Water	0.5	0.5–100	11	No	—	[49]
MSPE-GC/MS/MS	3D-rGOPFH	Vegetables		5–100 ng·g^{-}	26	No	10	[50]
MSPE-LC/MS/MS	Fe_3O_4-PSA	Grains	0.32	2–250	7	No	—	[51]
MSPE-GC/ECD	Fe-ACF/CNF	Water	4.08	20–500	16	No	4	[52]
MSPE-LC/MS/MS	Fe_3O_4-SiO_2	Earthworm	1	2–200	23	No	—	[53]
SPME-GC/MS	MIL-53(Al)/Fe_2O_3	Water	0.8	3–800	35	No	—	[54]
MSPE- GC/MS	Fe_3O_4@SiO_2-Apt	Plasma	0.46	2–700	10	Yes	15	This work

MVP-DB: magnetic polymer (*N*-vinyl pyrrolidone-divinyl benzene). MNPCs: magnetic nanoporous carbons. R-DSPE: reversed dispersive solid-phase extraction. CFR: catechol formaldehyde resin. GO: graphene oxide. 3D-rGOPFH: three-dimensional microporous reduced graphene oxide/polypyrrole nanotube/magnetite hydrogel. PSA: 3-(*N*,*N*-diethylamino)propyltrimethoxysilane. ACF/CNF: iron nanoparticles dispersed hierarchical carbon fiber forest.

good extraction performance and expanding the application range of MSPE methods. Another notable feature of this method is its reusability. Among the studies that provided this information, this material demonstrated the highest number of reuses, effectively reducing the cost of synthesis and usage. This method is similar to other methods reported in the literature in terms of adsorption time, detection limit, and linear range and can be used to analyze and detect phorate at trace levels. The comparison results demonstrate that the method has good selectivity, strong anti-interference ability, simple operation, high sensitivity, and environmental friendliness, making it suitable for specific detection of phorate in plasma samples and replacing existing methods for phorate extraction and detection in water environments.

4 Conclusion

In this study, Fe_3O_4@SiO_2-Apt MNPs were synthesized using a self-assembly method, combining Apt and MNPs, and characterized using SEM, FTIR, CLSM, and other techniques. The characterization results have confirmed the successful attainment of the desired outcomes at each step of the preparation process. This substantiates that the synthesized Fe_3O_4@SiO_2-Apt MNPs displayed favorable characteristics in terms of morphology, dispersion, stability, and magnetic responsiveness. By using this material as the sorbent, we established a magnetic dispersive solid-phase extraction method to effectively enrich and extract phorate from plasma samples. Subsequently, phorate was detected using GC-MS. Under the optimal extraction and elution conditions, the method's detection limit (S/N = 3) was $0.46\,\text{ng·mL}^{-1}$, accompanied by good repeatability. The analytical method proved to be reliable for the trace detection of phorate in samples. Comprehensive experimental results highlighted the method's advantages, including straightforward operation, short extraction time (10 min), strong specificity, high extraction efficiency (EF = 416), and excellent reusability (≥15 times). This method can be effectively applied for the extraction and detection of phorate in actual plasma samples, yielding acceptable recovery rates. Based on the method of combining aptamer and MSPE proposed in this study, it is expected to achieve selective extraction and detection of other kinds of target substances in biological samples by changing the type of Apt or utilizing the synergistic working approach of multiple Apt, which has a wide application prospect.

Funding information: This work was financially supported by the Opening Project of Key Laboratory of Evidence Science (China University of Political Science and Law), Ministry of Education (2019KFKT01), the National Natural Science Foundation of China (81871523), Scientific Research Foundation of Hebei North University(3050102003), and the Fundamental Research Funds for the Central Universities.

Author contributions: Ting Wang: writing – original draft, writing – review and editing, and investigation; Junpeng Tan: writing – original draft and data curation; Shenghui Xu: investigation and formal analysis; Yong Li: formal analysis and supervision; Hongxia Hao: writing – review and editing, project administration, and supervision.

Conflict of interest: The authors state no conflict of interest.

Data availability statement: The datasets generated during and/or analyzed during the current study are available from the corresponding author on reasonable request.

References

[1] Dar MA, Baba ZA, Kaushik G. A review on phorate persistence, toxicity and remediation by bacterial communities. Pedosphere. 2022;32(1):171–83. doi: 10.1016/S1002-0160(21)60043-7.

[2] Figueroa-Villar JD, Petronilho EC, Kuca K, Franca TCC. Review about structure and evaluation of reactivators of acetylcholinesterase inhibited with neurotoxic organophosphorus compounds. Curr Med Chem. 2021;28(7):1422–42. doi: 10.2174/0929867327666200425213215.

[3] Zhao M, Chen LH, Zhang ZG, Li C. New progress in the mechanism and treatment of organic phosphorus pesticide poisoning. Chin J Pract Intern Med. 2014;34(11):1064–8. doi: 10.7504/nk2014100205.

[4] Zhu J, Wang J, Ding Y, Liu B, Xiao W. A systems-level approach for investigating organophosphorus pesticide toxicity. Ecotoxicol Env Saf. 2018;149:26–35. doi: 10.1016/j.ecoenv.2017.10.066.

[5] Derbalah A, Chidya R, Jadoon W, Sakugawa H. Temporal trends in organophosphorus pesticides use and concentrations in river water in Japan, and risk assessment. J Environ Sci. 2019;79:135–52. doi: 10.1016/j.jes.2018.11.019.

[6] Khademi SMS, Salemi A, Jochmann M, Joksimoski S, Telgheder U. Development and comparison of direct immersion solid phase micro extraction Arrow-GC-MS for the determination of selected pesticides in water. Microchem J. 2021;164:106006. doi: 10.1016/j.microc.2021.106006.

[7] Iqbal S, Iqbal MM, Javed M, Bahadur A, Liu G. Modified QuEChERS extraction method followed by simultaneous quantitation of nine multi-class pesticides in human blood and urine by using GC-MS. J Chromatogr B. 2020;1152:122227. doi: 10.1016/j.jchromb.2020.122227.

[8] Notardonato I, Salimei E, Russo MV, Avino P. Simultaneous determination of organophosphorus pesticides and phthalates in baby food samples by ultrasound-vortex-assisted liquid–liquid microextraction and GC-IT/MS. Anal Bioanal Chem. 2018;410(14):3285–96. doi: 10.1007/s00216-018-0986-x.

[9] Wu L, Song Y, Hu M, Zhang H, Yu A, Yu C, et al. Application of magnetic solvent bar liquid-phase microextraction for determination of organophosphorus pesticides in fruit juice samples by gas chromatography mass spectrometry. Food Chem. 2015;176:197–204. doi: 10.1016/j.foodchem.2014.12.055.

[10] Chisvert A, Cárdenas S, Lucena R. Dispersive micro-solid phase extraction. Trends Anal Chem. 2019;112:226–33. doi: 10.1016/j.trac.2018.12.005.

[11] Cruz FV, Maria F, Grosso PJ, Maria OJ, Fernandes DV, Cristina DM. Magnetic dispersive micro solid-phase extraction and gas chromatography determination of organophosphorus pesticides in strawberries. J Chromatogr A. 2018;1566:1–12. doi: 10.1016/j.chroma.2018.06.045.

[12] Montiel-León JM, Duy SV, Munoz G, Verner MA, Hendawi MY, Moya H, et al. Occurrence of pesticides in fruits and vegetables from organic and conventional agriculture by QuEChERS extraction liquid chromatography tandem mass spectrometry. Food Control. 2019;104:74–82. doi: 10.1016/j.foodcont.2019.04.027.

[13] Badawy SM. Optimization of reaction time for detection of organophosphorus pesticides by enzymatic inhibition assay and mathematical modeling of enzyme inhibition. J Environ Sci Health B. 2021;56(2):142–9. doi: 10.1080/03601234.2020.1853455.

[14] Du L, Wang X, Liu T, Li J, Wang H. Magnetic solid-phase extraction of organophosphorus pesticides from fruit juices using NiFe2O4@polydopamine@Mg/Al-layered double hydroxides nanocomposites as an adsorbent. Microchem J. 2019;150:104128. doi: 10.1016/j.microc.2019.104128.

[15] Chahkandi M, Amiri A, Arami SRS. Extraction and preconcentration of organophosphorus pesticides from water samples and fruit juices utilizing hydroxyapatite/Fe3O4 nanocomposite. Microchem J. 2019;144:261–9. doi: 10.1016/j.microc.2018.09.018.

[16] Kumar N, Narayanan N, Gupta S. Ultrasonication assisted extraction of chlorpyrifos from honey and brinjal using magnetic molecularly imprinted polymers followed by GLC-ECD analysis. React Funct Polym. 2019;135:103–12. doi: 10.1016/j.reactfunctpolym.2018.12.012.

[17] Wang J, Mou ZL, Duan HL, Ma SY, Zhang J, Zhang ZQ. A magnetic hyperbranched polyamide amine-based quick, easy, cheap, effective, rugged and safe method for the detection of organophosphorus pesticide residues. J Chromatogr A. 2019;1585:202–6. doi: 10.1016/j.chroma.2018.11.071.

[18] Wang P, Luo M, Liu D, Zhan J, Liu X, Wang F, et al. Application of a magnetic graphene nanocomposite for organophosphorus pesticide extraction in environmental water samples. J Chromatogr A. 2018;1535:9–16. doi: 10.1016/j.chroma.2018.01.003.

[19] Hamedi R, Aghaie ABG, Hadjmohammadi MR. Magnetic core micelles as a nanosorbent for the efficient removal and recovery of three organophosphorus pesticides from fruit juice and environmental water samples. J Sep Sci. 2018;41(9):2037–45. doi: 10.1002/jssc.201701090.

[20] Torabi E, Moghadasi M, Mirzaei M, Amiri A. Nanofiber-based sorbents: Current status and applications in extraction methods. J Chromatogr A. 2023;1689:463739–15. doi: 10.1016/j.chroma.2022.463739.

[21] Torabi E, Mirzaei M, Bazargan M, Amiri A. A critical review of covalent organic frameworks-based sorbents in extraction methods. Anal Chim Acta. 2022;1224:340207–27. doi: 10.1016/j.aca.2022.340207.

[22] Bazargan M, Ghaemi F, Amiri A, Mirzaei M. Metal–organic framework-based sorbents in analytical sample preparation. Coord Chem Rev. 2021;224:214107–31. doi: 10.1016/j.ccr.2021.214107.

[23] Tang Q, Wang X, Yu F, Qiao X, Xu Z. Simultaneous determination of ten organophosphate pesticide residues in fruits by gas chromatography coupled with magnetic separation. J Sep Sci. 2014;37(7):820–7. doi: 10.1002/jssc.201301161.

[24] Mahpishanian S, Sereshti H. Three-dimensional graphene aerogel-supported iron oxide nanoparticles as an efficient adsorbent for magnetic solid phase extraction of organophosphorus pesticide residues in fruit juices followed by gas chromatographic determination. J Chromatogr A. 2016;1443:43–53. doi: 10.1016/j.chroma.2016.03.046.

[25] Li D, He M, Chen B, Hu B. Metal organic frameworks-derived magnetic nanoporous carbon for preconcentration of organophosphorus pesticides from fruit samples followed by gas chromatography-flame photometric detection. J Chromatogr A. 2019;1583:19–27. doi: 10.1016/j.chroma.2018.11.012.

[26] Pichon V, Brothier F, Combès A. Aptamer-based-sorbents for sample treatment—a review. Anal Bioanal Chem. 2015;407(3):681–98. doi: 10.1007/s00216-014-8129-5.

[27] Jin C, Qiu L, Li J, Fu T, Zhang X, Tan W. Cancer biomarker discovery using DNA aptamers. Analyst. 2016;141(2):461–6. doi: 10.1039/c5an01918d.

[28] Sun C, Sun R, Chen Y, Tong Y, Zhu J, Bai H, et al. Utilization of aptamer-functionalized magnetic beads for highly accurate fluorescent detection of mercury (II) in environment and food. Sens Actuators B Chem. 2018;255:775–80. doi: 10.1016/j.snb.2017.08.004.

[29] Frohnmeyer E, Frisch F, Falke S, Betzel C, Fischer M. Highly affine and selective aptamers against cholera toxin as capture elements in magnetic bead-based sandwich ELAA. J Biotechnol. 2018;269:35–42. doi: 10.1016/j.jbiotec.2018.01.012.

[30] Saberi Z, Rezaei B, Khayamian T. A fluorescent aptasensor for analysis of adenosine triphosphate based on aptamer–magnetic nanoparticles and its single-stranded complementary DNA labeled carbon dots. Luminescence. 2018;33(4):640–6. doi: 10.1002/bio.3457.

[31] Presnell KV, Alper HS. Thermodynamic and first-principles biomolecular simulations applied to synthetic biology: promoter and aptamer designs. Mol Syst Des Eng. 2018;3(1):19–37. doi: 10.1039/c7me00083a.

[32] Huang R, Xi Z, He N. Applications of aptamers for chemistry analysis, medicine and food security. Sci China Chem. 2015;58(7):1122–30. doi: 10.1007/s11426-015-5344-7.

[33] Li Y, Zhao M, Wang H. Label-free peptide aptamer based impedimetric biosensor for highly sensitive detection of TNT with a ternary assembly layer. Anal Bioanal Chem. 2017;409(27):6371–7. doi: 10.1007/s00216-017-0576-3.

[34] Farzin L, Shamsipur M, Sheibani S. A review: Aptamer-based analytical strategies using the nanomaterials for environmental and human monitoring of toxic heavy metals. Talanta. 2017;174:619–27. doi: 10.1016/j.talanta.2017.06.066.

[35] Wang L, Liu X, Zhang Q, Zhang C, Liu Y, Kang T, et al. Selection of DNA aptamers that bind to four organophosphorus pesticides. Biotechnol Lett. 2012;34(5):869–74. doi: 10.1007/s10529-012-0850-6.

[36] Zhang C, Wang L, Tu Z, Sun X, He Q, Lei Z, et al. Organophosphorus pesticides detection using broad-specific single-stranded DNA based fluorescence polarization aptamer assay. Biosens Bioelectron. 2014;55:216–9. doi: 10.1016/j.bios.2013.12.020.

[37] Pang S, Labuza TP, He L. Development of a single aptamer-based surface enhanced raman scattering method for rapid detection of multiple pesticides. Analyst. 2014;139:1895–901. doi: 10.1039/c3an02263c.

[38] Bai W, Zhu C, Liu J, Yan M, Yang S, Chen A. Gold nanoparticle-based colorimetric aptasensor for rapid detection of six organophosphorous pesticides. Environ Toxicol Chem. 2015;34(10):2244–9. doi: 10.1002/etc.3088.

[39] Shen Z, Xu D, Wang G, Geng L, Xu R, Wang G, et al. Novel colorimetric aptasensor based on MOF-derived materials and its applications for organophosphorus pesticides determination. J Hazard Mater. 2022;440:129707. doi: 10.1016/j.jhazmat.2022.129707.

[40] Tang T, Deng J, Zhang M, Shi G, Zhou T. Quantum dot-DNA aptamer conjugates coupled with capillary electrophoresis: a universal strategy for ratiometric detection of organophosphorus pesticides. Talanta. 2016;146:55–61. doi: 10.1016/j.talanta.2015.08.023.

[41] Li X, Shi J, Chen C, Li W, Han L, Lan L, et al. One-step, visual and sensitive detection of phorate in blood based on a DNA–AgNC aptasensor. N J Chem. 2018;42(8):6293–8. doi: 10.1039/c8nj00958a.

[42] Dou X, Chu X, Kong W, Luo J, Yang M. A gold-based nanobeacon probe for fluorescence sensing of organophosphorus pesticides. Anal Chim Acta. 2015;891:291–7. doi: 10.1016/j.aca.2015.08.012.

[43] Li H, Huang X, Huang J, Bai M, Hu M, Guo Y, et al. Fluorescence assay for detecting four organophosphorus pesticides using fluorescently labeled aptamer. Sensors. 2022;22:5712. doi: 10.3390/s22155712.

[44] Deng H, Li X, Peng Q, Wang X, Chen J, Li Y. Monodispherse magnetic single-crystal ferrite microspheres. Angew Chem. 2005;44(18):2782–5. doi: 10.1002/anie.200462551.

[45] Yang Y, Su P, Zheng K, Wang T, Song J, Yang Y. A self-directed and reconstructible immobilization strategy: DNA directed immobilization of alkaline phosphatase for enzyme inhibition assays. RSC Adv. 2016;6:36849–56. doi: 10.1039/c6ra01621a.

[46] Zhang S, Zhang W, Dai J, Sun M, Zhao J, Ji L, et al. Carboxylated carbon nanotubes with high electrocatalytic activity for oxygen evolution in acidic conditions. InfoMat. 2022;4:e12273. doi: 10.1002/inf2.12273.

[47] Liu Z, Wang J, Wang Z, Xu H, Di S, Zhao H, et al. Development of magnetic solid phase extraction using magnetic amphiphilic polymer for sensitive analysis of multi-pesticides residue in honey. J Chromatogr A. 2022;1664:462789. doi: 10.1016/j.chroma.2021.462789.

[48] Khetagoudar MC, Jinendra U, Kumar AP, Bilehal D, Kollur SP. Multiresidue pesticide analysis in green chilli using GC–MS/MS using modified QuEChERS method with highly efficient Fe_3O_4@CFR@GO nanocomposite. Inorg Chem Commun. 2022;137:109195. doi: 10.1016/j.inoche.2022.109195.

[49] Srivastava N, Kumari S, Nair K, Alam S, Raza SK. Determination of organophosphorous pesticides in environmental water samples using surface-engineered C18 functionalized silica-coated core-shell magnetic nanoparticles–based extraction coupled with GC-MS/MS analysis. J AOAC Int. 2017;100(3):804–9. doi: 10.5740/jaoacint.16-0312.

[50] Wang S, Li X, Li M, Li X, Li X, Li S, et al. Self-assembled three-dimensional microporous rGO/PNT/Fe_3O_4 hydrogel sorbent for magnetic preconcentration of multi-residue insecticides. Appl Sci. 2020;10:5665. doi: 10.3390/app10165665.

[51] Liu Z, Qi P, Wang X, Wang Z, Xu X, Chen W, et al. Multi-pesticides residue analysis of grains using modified magnetic nanoparticle adsorbent for facile and efficient cleanup. Food Chem. 2017;230:423–31. doi: 10.1016/j.foodchem.2017.03.082.

[52] Singh M, Pandey A, Singh S, Singh SP. Iron nanoparticles decorated hierarchical carbon fiber forest for the magnetic solid-phase extraction of multi-pesticide residues from water samples. Chemosphere. 2021;282:131058. doi: 10.1016/j.chemosphere.2021.131058.

[53] Sun Y, Qi P, Cang T, Wang Z, Wang X, Yang X, et al. High-throughput multipesticides residue analysis in earthworms by the improvement of purification method: development and application of magnetic Fe_3O_4-SiO_2 nanoparticles based dispersive solid-phase extraction. J Sep Sci. 2018;41:2419–31. doi: 10.1002/jssc.201701296.

[54] Moinfar S, Khodayari A, Sohrabnezhad S, Aghaei A, Jamil LA. MIL-53(Al)/Fe_2O_3 nanocomposite for solid-phase microextraction of organophosphorus pesticides followed by GC-MS analysis. Mikrochim Acta. 2020;187:647. doi: 10.1007/s00604-020-04621-z.